Tensile properties of Co-added FeCrAl oxide dispersion strengthened alloy

Shenghua ZHANG[1*], Shigeharu UKAI[2], S.M.S. AGHAMIRI[2], Naoko OONO[2] and Shigenari HAYASHI[2]

[1]*Graduate School of Engineering, Hokkaido University, Kita 13, Nishi 8, Kita-ku, Sapporo 060-8628, Japan*

[2]*Faculty of Engineering, Hokkaido University, Kita 13, Nishi 8, Kita-ku, Sapporo 060-8628, Japan*

* Corresponding author: Shenghua ZHANG e-mail: shenghzhang_989@163.com

Abstract

The Co-added FeCrAl oxide-dispersion-strengthened (ODS) alloy developed by the authors enables easy and precise control of the grain morphology and hardness using α/γ phase transformation during manufacturing. The tensile properties of the transformable Co-added FeCrAl-ODS alloy were evaluated, focusing on the oxide dispersion strengthening and B2-type CoAl ordered strengthening at both ambient and elevated temperatures. The oxide particles and B2-type CoAl precipitate were characterized using transmission electron microscopy, and strengthening mechanisms for the oxide particles and CoAl-precipitate were evaluated by hardness and tensile tests at room temperature, 300 °C, and 500 °C. The theoretically estimated values showed good agreement with the experimental results at RT and 300 °C. However, the order strengthening by CoAl precipitates was significantly reduced at 500 °C, which was attributed to the increase of thermally activated ⟨001⟩ slip in the body-centered cubic matrix. The ⟨001⟩ slip weakened the dislocation interaction with CoAl precipitates with the same ⟨001⟩ slip system.

Keywords: FeCrAl; ODS; Cobalt addition; Aging treatment; Mechanical properties; Order strengthening

1. Introduction

FeCr ferritic steels exhibit high thermal conductivity with a low thermal expansion coefficient [1-3], leading to their widespread used in many industries where high temperature oxidation resistance is needed, such as steam-containing environments in thermal power plants [4, 5]. Since the severe accident of Fukushima Daiichi nuclear power plant on March 11, 2011, the development of oxidation-resistant alloys for accident-tolerant fuel (ATF) cladding has been focused worldwide. In the United States, FeCrAl alloys have been studied [6-10] because Al-containing alloys produce stable alumina (Al_2O_3) scale, preventing direct reaction of Fe with steam. In Japan, FeCrAl oxide dispersion strengthened (ODS) alloys with improved high-temperature strength contributed by nano-sized oxide particles have been developed for additional radiation tolerance [11, 12] based on the previous research and development of 9Cr-ODS [13-15], 12Cr-ODS [16-18], and high Cr-ODS [19] for Generation IV fast reactors.

So far the studies on the oxidation behavior and mechanical properties of FeCrAl ODS alloys have been working on [20-22]. The standard composition of FeCrAl ODS alloys is Fe–12Cr–6Al–0.4Zr–0.5Ti–0.24Ex.O–0.5Y_2O_3 (wt.%), where Ex.O (excess oxygen) means the total oxygen minus oxygen coupled with yttrium as Y_2O_3. The standard FeCrAl alloy contains a large amount of the ferrite former elements Cr and Al to improve the corrosion and oxidation resistance, which results in a full ferrite structure until melting. The grain morphology and hardness of FeCrAl ODS alloys can thus be controlled only by recovery and recrystallization during the intermediate heat treatment in cladding manufacturing by pilger mill rolling. In contrast, with the development of transformable FeCrAl ODS alloys, the grain morphology and hardness can be controlled by γ/α phase transformation more easily and precisely during the intermediate heat treatment [23]. These transformable FeCrAl ODS alloys are being developed by the authors by introducing the austenite former elements Ni [24] or Co [25]; no other groups are currently working on such a study. For Co-added FeCrAl ODS alloys, the nominal composition Fe–12Cr–5Al–25Co–0.5Y_2O_3 (wt.%) was optimized from the viewpoint of γ/α phase transformation and oxidation resistance [25]. The thermal neutron cross section of the (n, γ) reaction for Co-59 with 100% natural abundance is 37.21 barn (b) from JENDL-4.0, which is much higher than that of the conventional light water reactor material Zr-90 (10.66 mb). Therefore, Co-added

FeCrAl ODS alloy cannot be applied to the nuclear field; however, it can be applied for other industries for which high-temperature strength and corrosion and oxidation resistance are required. In this study, the tensile properties of the optimized Co-added FeCrAl ODS alloy were investigated, focusing on the oxide dispersion strengthening and order strengthening by B2-type CoAl intermetallic compound at both ambient and elevated temperatures.

2. Experimental method

Fe–12Cr–5Al–25Co–0.5Y_2O_3 (FCACO) alloy was fabricated using the following processes. High-purity powders of iron, chromium, cobalt, yttria, and 50Al–50Fe alloy were mixed in a sealed stainless-steel pot and mechanically alloyed (MAed) under argon gas atmosphere. The MAed powders were then consolidated by spark plasma sintering [25]. Using X-ray fluorescence analysis, the chemical composition of the manufactured specimen was measured to be Fe–11.38Cr–4.74Al–22.97Co–0.45Y_2O_3 (wt.%). The sintered specimens were then subjected to hot rolling at 1150 °C with a total thickness reduction of 80%. The final homogenization was performed at 1150 °C for 1 h, and the specimens were then air cooled to room temperature. According to the phase diagram (**Fig. 1**) and phase transformation temperature given in ref. [25], the B2-type CoAl precipitate dissolves into the matrix at approximately 800 °C, and ferrite is stable below the A_{C1} temperature of 880 °C; thus, the solution treatment consisted of holding at 850 °C for 1 h followed by quenching in 15 °C water. Aging treatment was conducted at different temperatures (400 °C, 500 °C, 550 °C, and 600 °C) for 100 h to determine the optimal aging treatment.

The Vickers hardness (VH) of each aged sample was obtained using a HMV microhardness tester (SHIMADZU, MCT series) under a load of 0.2 kgf with a dwell time of 15 s, with 5 measurements for each sample. The tensile test was performed at room temperature (RT), 300 °C, and 500 °C at a strain rate of 1×10^{-3} s^{-1} using a universal material testing machine (SHIMADZU, AG-X-20kN). Miniaturized tensile specimens were prepared with gauge dimensions of 5 mm in length, 1.2 mm in width, and 0.5 mm in thickness using an electro-discharge processing machine. The fracture surfaces of the tensile samples were examined using field-emission scanning electron microscopy (FE-SEM, JEOL JSM-6500F). The distribution of oxide particles and CoAl

precipitates in the aged specimens were analyzed using transmission electron microscopy (TEM, 200kV-JEOL JEM-2010 and 300kV-FEI Titan G2), and ~100nm-thick specimens were prepared using focused ion beam milling combined with FE-SEM (FIB-SEM, JEOL JIB-4601F). To study the dislocations in the tensile samples, TEM specimens near the fractures were prepared by FIB-SEM and characterized using the two-beam condition (200 kV) to observe dislocations with different g-vectors. The size of the CoAl precipitates and oxide particles were measured using image processing software (ImageJ 1.48v).

3. Results

3.1 Distribution of CoAl precipitates and oxide particles

The specimens were solution treated at 850 °C for 1 h and then quenched in water, resulting in the dissolution of the CoAl precipitates into the matrix. The average VH with error bars indicating the maximum and minimum are shown in **Fig. 2**. The initial hardness is 430 HV, and the evolution of VH is plotted as a function of aging time at 400 °C, 500 °C, 550 °C, and 600 °C. VH sharply increased at the beginning of aging within 20 h; thereafter, the increasing tendency became moderate and saturated. The VH of the 600 °C-aging-treated specimen (600-AT) started to decrease after 20 h. Consequently, 550 °C and 20 h are the optimal aging temperature and aging time in this work. The VH decrease of 600-AT could be due to CoAl phase coarsening. To confirm this behavior, CoAl precipitates in the 550 °C-20h-aging-treated specimen (550-20-AT) and 600-100-AT were observed using a Titan transmission electron microscope (Titan-TEM).

In **Fig. 3**, although it is difficult to find a Co or Al concentrated zone to distinguish CoAl precipitates because of the small size and overlap, Cr-depleted zones are apparent because of the CoAl precipitation. In other words, the presence of CoAl precipitates was confirmed in Cr-depleted zones, and some zones mixed with blue and yellow color in Co–Al dual elemental mappings also corresponded to the position of Cr-depleted zones, as observed in the circled zone. The statistics indicate that the average diameter of the CoAl precipitates in 550-20-AT is approximately 7 nm. The concentrated zones in the Co and Al elemental mappings of 600-100-AT in **Fig. 4** are more obvious than those in 550-20-AT. The Co and Al concentrated zones are easily noticed and are well mixed in

the Co-Al dual elemental mapping. As expected, the average diameter of CoAl precipitates in 600-100-AT is 46 nm, which is much larger than that in 550-20-AT.

The distribution of oxide particles was also examined using TEM, as shown in **Fig. 5**. The black spots of smaller size are Y_2O_3 particles, and they are abundantly and uniformly dispersed in the alloys. A few larger particles are also observed, and they are considered to be Y–Al–O ($YAlO_3$ and $Y_3Al_5O_{12}$) complex oxides [26]. The larger size of Y–Al–O complex oxides is attributed to their higher interfacial energy and higher solubility of Al in the matrix [27, 28]. The diameters of most of the oxide particles are distributed in the range of 3–9 nm and the average diameter is 6 nm according to a previous study [25].

3.2 Structure of CoAl precipitates and ferrite matrix

An inverse pole figure (IPF) map and the corresponding grain boundary map for 550-20-AT are presented in **Fig. 6**, implying that the matrix is ferrite with a body-centered cubic (bcc) structure in an average grain size (GS) of 1.60 μm transformed from austenite during air cooling. The electron diffraction patterns of the ferrite matrix and precipitates are presented in **Fig. 7**. The lattice constants were derived from analysis of the diffraction patterns. The calculated lattice constant of the ordered B2 phase, a_{B2}, and matrix, a_{bcc}, are summarized in **Table 1**. These constants**,** a_{B2} and a_{bcc}, are only 0.1-Å higher than those reported in the literature [29, 30], which could be caused by the error from TEM observation. The misfit strain between the matrix and ordered B2 phase was calculated using the formula of $\delta = 2\times(a_{B2}-a_{bcc})/(a_{B2}+a_{bcc})$. The calculated value of δ is also shown in **Table 1**. The misfit strain between the B2-type precipitates and ferrite matrix is only 0.24%, implying that coherency is extremely high and that it is important to consider the strengthening mechanism by B2-type precipitates.

3.3 Tensile properties

Fig. 8 presents the stress–strain (S–S) curves of 550-20-AT at RT, 300 °C, and 500 °C. The tensile tests were conducted two times at each temperature. The yield strength (YS) and ultimate tensile strength (UTS) at room temperature are approximately 1600 MPa and decrease with increasing testing temperature. The uniform

elongation (UE) and total elongation (TE) were also measured; the total elongation clearly increases with increasing temperature. The average values of the tensile data at different temperatures are summarized in **Table 2**.

Fig. 9 shows the fracture surfaces of the tensile specimens at RT, 300 °C, and 500 °C. Numerous river patterns are observed in the RT specimen, which is the typical fracture mode exhibited in transgranular fracture. The formation of these river patterns was a result of a cleavage crack crossing a twist boundary between grains. Upon increasing the temperature to 300 °C, the number of river patterns decreased, whereas that of cracks on the fracture surface increased. The specimen tested at 500 °C exhibits a cup-and-cone fracture surface and numerous spherical "dimples" are clearly observed when it was examined at higher magnification. Each dimple is one half of a microvoid that formed and then separated during the fracture process. Generally, the ductile alloy presents a cup-and-cone fracture surface, which shows agreement with the ductility increase for 500 °C tensile specimen.

4. Discussion

4.1 Oxide particle strengthening (σ_o) and B2-type order strengthening (σ_{order})

One of the strengthening factors in Co-added FeCrAl-ODS alloy comes from the dispersed oxide particles shown in **Fig. 5**. The oxide particles interact with the moving dislocations via the Orowan mechanism [31]. σ_o is the threshold stress and corresponds to the oxide-particle hardening stress, which is expressed in terms of the critical resolved shear stress (CRSS), τ_o, by the Orowan mechanism and the Taylor factor, M, 3.06.

$$\sigma_o = M \times \tau_o \tag{1}$$

$$\tau_o = A\frac{1}{2\pi}\frac{Gb}{\lambda}\left(\ln\frac{D}{r_0} + B_0\right) \tag{2}$$

$$\lambda = 1.25l_s - 2r_s \tag{3}$$

$$l_s = \sqrt{\frac{2\pi\overline{r^3}}{3f\bar{r}}} \tag{4}$$

$$r_s = \frac{\pi\overline{r^2}}{4\bar{r}} \tag{5}$$

where G is the shear modulus of the matrix (78.0 GPa at RT, 71.1 GPa at 300 °C, and 64.3 GPa at 500 °C) [32]; b is the magnitude of the burgers vector (2.48×10^{-10} m); λ is the average face-to-face distance between two particles; r_o is the inner cut-off radius of a dislocation core, which is taken to range from b to $3b$; D is the harmonic mean of λ and $2r_s$; $\bar{r}$ is the average oxide particle radius obtained from TEM micrographs (**Fig. 5**); and $\overline{r^2}$ and $\overline{r^3}$ are the averages of r^2 and r^3, respectively. r_s is the equivalent average particle radius and l_s is the average center to center distance. The volume fraction, f, of the oxide particles was evaluated using TEM bright field images. For a screw dislocation, B_0 is 0.6, and A is a constant given by the following equations [31, 32]:

$$A = 1/(1-v) \tag{6}$$

$$v = 4.46\times10^{-5}T + 0.27. \tag{7}$$

Here, v is Poisson's ratio and T is temperature expressed in °C. The detailed parameters for the calculation are listed in **Table 3**, and the oxide-particle hardening stress, σ_o, values estimated using the above parameters are summarized in **Table 4**, where the range of σ_o is attributed to uncertainty of the cut-off radius of a dislocation core ranging from b to $3b$.

The increase of the VH after aging at 550 °C for 20 h resulting from B2-type CoAl precipitates could be approximately converted into the increase of the ultimate tensile strength (ΔUTS) using the following empirical relationship [33]:

$$\Delta UTS(MPa) = \Delta Hv(MPa)/3. \tag{8}$$

Here, ΔHv was measured to be 1274 MPa (130 kgf/mm^2) from **Fig. 2**, which corresponded to 425 MPa for ΔUTS. As shown in **Table 1**, the B2-type CoAl particles are an ordered phase and maintained excellent coherency with the matrix. When dislocations shear precipitates, the possible strengthening mechanisms that are generally considered are coherency strengthening, modulus mismatch strengthening, and order strengthening. For CoAl precipitates with the B2-type ordered phase maintaining excellent coherency with the matrix, Yasuda et al. confirmed that the dominant strengthening mechanism was order strengthening [34]. B2-type ordered particles are

sheared by moving dislocations, and the CRSS for the order strengthening is expressed by the following equation [35]:

$$\tau_{\text{order}}(1) = \frac{\gamma_{\text{APB}}}{2b}\left[\left(\frac{\gamma_{\text{APB}} rf}{T}\right)^{\frac{1}{2}} - f\right]. \quad (9)$$

In addition, Ardell [36] modified the above equation as follows:

$$\tau_{\text{order}}(2) = \frac{\gamma_{\text{APB}} u}{2b} \quad (10)$$

$$u = \frac{(4B + B^2/3)^2 - B}{2(1 - B/6)} \quad (11)$$

$$B = \frac{3\pi^2 \gamma_{\text{APB}} fr}{32T}, \quad (12)$$

where γ_{APB} is the anti-phase boundary (APB) energy per unit area, taken as 750 MJ/m^2, and T is the line tension of a dislocation, approximately equal to $Gb^2/2$, where the values of G are same as those mentioned above. The volume fraction f of precipitates and the average precipitate radius r were determined from TEM images using quantitative stereology. These values were listed in **Table 3**. The order strengthening stress σ_{order} is obtained by multiplying by the Taylor factor M (3.06) and the constant α for the CRSS:

$$\sigma_{\text{order}} = \alpha \times M \times \tau_{\text{order}}. \quad (13)$$

τ_{order} (1) was estimated to be 369 MPa according to Eq. (9), and τ_{order} (2) was calculated to be 442 MPa using Eq. (10); σ_{order} for RT was 425 MPa (Δ *UTS*); thus α (1) and α (2) were calculated to be 0.38 and 0.31 respectively. Then, the value of σ_{order} for 300 °C and 500 °C were derived. **Table 4** presents the calculation results for the order strengthening σ_{order} (1) and σ_{order} (2) together with those of the oxide dispersion strengthening σ_{o}.

The temperature dependencies of the order strengthening and oxide dispersion strengthening are schematically illustrated in **Fig. 10**. The YS results shown as black squares and connected with solid black lines are the experimental tensile test results at RT, 300 °C, and 500 °C; the oxide dispersion strengthening σ_{o} and order strengthening σ_{order}, calculated using Eq. (1) and Eq. (13), are indicated by the bars in cyan and yellow,

respectively. Yamamoto et al. [37] reported the tensile properties of FeCrAl alloys without Y_2O_3 addition (FCA alloys) from RT to 550 °C. The YS data at RT, 300 °C, and 500 °C from that study are presented with triangles and connected with dashed blue lines in **Fig. 10**. Massey et al. [38] studied the tensile properties of FeCrAl ODS alloys (FCAO alloys) from RT to 800 °C with similar chemical composition and grain size as the authors' specimen. Their YS results are indicated by circles and dashed red lines in **Fig. 10**. The differences in YS between the FCA and FCAO alloys are attributed to the oxide dispersion strengthening σ_o, which is consistent with the values of strengthening stress estimated using Eq. (1) and shown in **Table 4**. Furthermore, the order strengthening σ_{order} by B2-type CoAl precipitates resulted in the difference in YS between the FCACO alloy and FCAO alloys, as there is no Co addition in FCAO alloys. This YS difference agrees well with the values of strengthening stress estimated using Eq. (13) and shown in **Table 4** at RT and 300 °C. When the temperature increases to 500 °C, however, this consistency broke down; the order strengthening σ_{order} by B2-type CoAl precipitates appeare to be significantly reduced as it is compared with the stress estimated using Eq. (13), as shown in **Fig. 10**, where the calculation result for the order strengthening σ_{order} at 500 °C is indicated by the hollow yellow bar.

4.2 B2-type order strengthening (σ_{order}) at 500 °C

In the followings, the reduction of the ordered stress σ_{order} by B2-type CoAl precipitates at 500 °C is considered. It is known that the favorable slip system of bcc metals is $\{110\}\langle 111\rangle$, whereas the primary slip system of B2-type CoAl precipitate is $\{010\}\langle 001\rangle$ [39]. The activation of $\langle 111\rangle$ slip in the CoAl precipitate is extremely difficult. Therefore, when a/2 $\langle 111\rangle$ dislocations in the bcc matrix pass through the CoAl B2 precipitates, the precipitates strongly suppress the dislocation motion, which is considered an origin of the order strengthening. Concerning $\langle 111\rangle$ and $\langle 001\rangle$ slip in bcc metals, Takeuchi [40] and Chin [41] reported that the CRSS for $\langle 001\rangle$ slip was at least $\sqrt{3}$ times higher than that for $\langle 111\rangle$ slip. Yasuda et al. [28] conducted compression tests on FeAlCo single crystals containing B2-type CoAl precipitates in various directions, and the Schmid factors for the $\langle 111\rangle$ and $\langle 001\rangle$ slip systems also changed with different loading directions. They stated that $\{010\}\langle 001\rangle$ slip can be induced by CoAl

precipitates in a bcc matrix because the Schmid factors of ⟨001⟩ slip were higher than those of ⟨111⟩ slip in some loading directions. Intermediate slip planes with ⟨001⟩ direction can also be thermally activated upon increasing the temperature to 450 °C ~ 550 °C, because their CRSS decreases more rapidly than that of typical {010}⟨001⟩ slip at those temperatures [34]. The ⟨001⟩ slip in the bcc matrix weakens the B2-type ordered strengthening because of the parallel slip with the CoAl-B2 phase.

The dislocation Burgers vectors in tensile specimens tested at 500 °C were then characterized by TEM to verify the possibility for ⟨001⟩ slip in the ferritic matrix. Bright-field TEM (BF-TEM) images of the tensile specimen tested at 500 °C are shown in **Fig. 11**, where four different g-vectors, $[110]$, $[1\bar{1}0]$, $[020]$, and $[200]$ near the $[001]$ zone axis were selected. Based on the visibility criteria ($|\vec{g}\cdot\vec{b}|$ values) given in **Table 5**, all the dislocations with the Burgers vectors of $\frac{a}{2}\langle 111\rangle$ and $a\langle 100\rangle$ were analyzed. Further analysis of the four figures indicated that the dislocations of the Burgers vectors of $a[100]$, $a[010]$, and $\frac{a}{2}\langle 111\rangle$ can be identified as indicated by the red, yellow, and blue arrows, respectively. In the top right area, a dislocation with a $[100]$ Burgers vector showed clear contrast in all the figures except for that with the $[020]$ g-vector. Two dislocations with $\frac{a}{2}\langle 111\rangle$ Burgers vectors located in the area below it were invisible in the figures with the $[110]$ g-vector and $[1\bar{1}0]$ g-vector individually. In the lower part of the figures, a dislocation possessing a $[010]$ Burgers vector showed weak contrast in the figure with the $[200]$ g-vector.

More than 200 dislocations were individually characterized for the tensile specimens tested at RT and 500 °C. The statistical results indicate that ⟨001⟩-type dislocations in the tensile specimens tested at RT accounted for approximately 6% of the dislocations, which is in good agreement with the result reported in the reference [42]; however, those in tensile specimens tested at 500 °C accounted for 13% of the dislocations, which is more than twice those in the RT tensile specimen. Therefore, it is worth noting that at approximately 500 °C, thermally activated ⟨001⟩ slip in the bcc ferrite can provide weak interaction with B2-type CoAl precipitates containing the same ⟨001⟩ slip. This situation is considered to be an origin of the decrease of the order strengthening at 500 °C.

As reported in the previous study [25], the FCACO presented γ/α phase transformation for efficient manufacture of FeCrAl ODS alloys. The results of mechanical properties reported in present study shows that the strength of FCACO is higher than that of Co free FeCrAl ODS alloys at the temperature lower than 500 °C. The strength of FCACO alloy and FCAO alloys becomes close at 500 °C as shown in **Fig. 10**, which is attributed to the failure of order strengthening. Thus, it is believed that the mechanical properties of FCACO alloy are similar as those of Co free FeCrAl ODS alloys at the temperature over 500 °C. Therefore, 25 wt.% Co addition is recommended in consideration of phase transformation and mechanical properties.

5. Conclusion

The hardness and tensile properties of Co-added FeCrAl ODS alloy containing oxide particles and B2-type CoAl precipitates were evaluated, focusing on the oxide particle dispersion strengthening and CoAl order strengthening at both ambient and elevated temperatures. The aging treatment condition for Fe–12Cr–5Al–25Co–0.5Y_2O_3 alloy was 20 h and 550 °C to optimize the formation of CoAl B2-type precipitates. The contributions of ODS and CoAl order strengthening were calculated, and the results reasonably agreed with the experimental results at RT and 300 °C. It was found, however, that the tensile strength contributed by the CoAl ordered precipitate was completely reduced at 500 °C. Through characterization of the dislocation Burgers vector in the specimens tested at RT and 500 °C, the abundance frequency of ⟨001⟩-type dislocations in the ferrite matrix was 13% in the 500 °C tensile specimens, which is more than twice that in the RT tensile specimens. Considering that the slip system of the B2-type CoAl phase was $\{010\}\langle 001\rangle$, the significant reduction of the order strengthening σ_{order} at 500 °C was attributed to the thermally activated ⟨001⟩ slip in the ferrite matrix, which provided weak interaction with B2-type CoAl precipitates with the same ⟨001⟩ slip.

Acknowledgments

S.H. Zhang would like to acknowledge the China Scholarship Council (CSC) for the provision of a scholarship. The EBSD and TEM analyses were performed at the “Joint-Use Facilities: Laboratory of Nano-Micro Material Analysis”, Hokkaido University.

References

[1] F. Masuyama, History of Power Plants and Progress in Heat Resistant Steels. ISIJ inter. 41 (2011) 612-625.

[2] F. Abe, Research and development of heat-resistant materials for advanced USC power plants with steam temperatures of 700 °C and above. Engineering 1 (2015) 211-224.

[3] H.K.D.H. Bhadeshia, Design of ferritic creep-resistant steels. ISIJ inter. 41 (2001) 626-640.

[4] E.A. Gulbransen, K.F. Andrew, Oxidation studies on the Iron-Chromium-Aluminum heater alloys. J. Electrochem. Soc. 106 (1959) 294-302.

[5] C.S. Wukusick, J.F. Collis, An iron-chromium-aluminum alloy containing yttrium. Mater. Res. Std. 4 (1964) 637-646.

[6] S.J. Zinkle, K.A. Terrani, J.C. Gehin, L.J. Ott, L.L. Snead, J. Nucl. Mater. 448 (2014) 374-379.

[7] K.A. Terrani, S.J. Zinkle, L.L. Snead, J. Nucl. Mater. 448 (2014) 420-435.

[8] Y. Yamamoto, B.A. Pint, K.A. Terrani, K.G. Field, Y. Yang, L.L. Snead, J. Nucl. Mater. 467 (2015) 703-716.

[9] K.G. Field, S.A. Briggs, K. Sridharan, R.H. Howard, Y. Yamamoto, J. Nucl. Mater. 489 (2017) 118-128.

[10] K.A. Terrani, Accident tolerant fuel cladding development: Promise, status, and Challenges, J. Nucl. Mater. 501 (2018) 13-30.

[11] S. Ukai, N. Oono, S. Ohtsuka, T. Kaito, K. Sakamoto, T. Torimaru, A. Kimura, S. Hayashi, Proceeding of LWR Fuel with Enhanced Safety and Performance, TOPFUEL2016, September 13, 2016, Boise, Idaho, USA.

[12] S. Ukai, N. Oono, K. Sakamoto, T. Torimaru, T. Kaito, A. Kimura, S. Hayashi, Proceedings of ICAPP, April 24-28, 2017, Fukui and Kyoto (Japan).

[13] M. Yamamoto, S. Ukai, S. Hayashi, T. Kaito, S. Ohtsuka, Reverse phase transformation from α to γ in 9Cr-ODS ferritic steels. J. Nucl. Mater. 417 (2011) 237–240.

[14] S. Ukai, S. Ohtsuka, T. Kaito, H. Sakasegawa, N. Chikata and S. Hayashi, High-Temperature Strength Characterization of Advanced 9Cr-ODS Ferritic Steels. Mater. Sci. Eng. A 510–511 (2009) 115–120.

[15] S. Ukai, S. Mizuta, M. Fujiwara, T. Okuda and T. Kobayashi, Development of 9Cr-ODS martensitic steel claddings for fuel pins by means of ferrite to austenite phase transformation. J. Nucl. Sci. Technol. 39 (2002) 778.

[16] B. Leng, S. Ukai, Y. Sugino, S. Tang, T. Narita, S. Hayashi, F. Wang. S. Ohtsuka and T. Kaito, Recrystallization texture of cold-rolled oxide dispersion strengthened ferritic steel. ISIJ Inter. 51 (2011) 951–957.

[17] T. Narita, S. Ukai, T. Kaito, S. Otsuka and T. Kobayashi, Development of two-step softening heat-treatment for manufacturing 12Cr-ODS ferritic steel tubes, J. Nucl. Sci. Technol. 41 (2004) 1008-1012.

[18] S. Ukai, T. Okuda, M. Fujiwara, T. Kobayashi, S. Mizuta, H. Nakashima, Characterization of high temperature creep properties in recrystallized 12Cr-ODS ferritic steel claddings, J. Nucl. Sci. Technol. 39 (2002) 872-879.

[19] A. Kimura, R. Kasada, N. Iwata, H. Kishimoto, C.H. Zhang, J. Isselin, P. Dou, J.H. Lee, N. Muthukumar, T. Okuda, M. Inoue, S. Ukai, S. Ohnuki, T. Fujisawa, F. Abe, Development of Al added high-Cr ODS steels for fuel cladding of next generation nuclear systems. J. Nucl. Mater. 417 (2011) 176–179.

[20] Y. Qiao, P. Wang, W. Qi, S. Du, Z. Liu, F. Meng, X. Zhang, K. Wang, Q. Li, Z. Yao, C. Bai, X. Wang, Mechanism of Al on FeCrAl steam oxidation behavior and molecular dynamics simulations. J. Alloys Compd. 828 (2020) 154310.

[21] S. Wu, J. Li, W. Li, S. Liu, Characterization of oxide dispersoids and mechanical properties of 14Cr-ODS FeCrAl alloys. J. Alloys Compd. 814 (2020) 152282.

[22] S.M.S. Aghamiri, T. Sowa, S. Ukai, N. Oono, K. Sakamoto, S. Yamashita, Microstructure and texture evolution and ring-tensile properties of recrystallized FeCrAl ODS cladding tubes. Mater. Sci. Eng. A 771 (2020) 138636.

[23] S. Ukai, S. Ohtsuka, T. Kaito, Y. de Carlan, J. Ribis, J. Malaplate, Structural Materials for Generation IV Nuclear Reactors. Woodhead publishing, Cambridge. 2017, pp. 357-414.

[24] T. Nishikawa, S. Zhang, S. Ukai, N. Oono, S. Hayashi, Development of α/γ transformable FeCrAl-ODS alloys by nickel addition. Mater. Trans. 60 (2019) 355-363.

[25] S.H. Zhang, S. Ukai, T. Nishikawa, S. M. S. Aghamiri, N. Oono, S. Hayashi, Development and characterization of γ/α transformable FeCrAl-ODS alloys by cobalt addition. J. Alloys Compd. 797 (2019) 390-398.

[26] M. Klimiankou, R. Lindau, A. Möslang, J. Schröde, TEM study of PM 2000 steel. Powder Metall. 48 (3) (2005) 277-287.

[27] N. Oono, S. Ukai, S. Hayashi, S. Ohtsuka, T. Kaito, A. Kimura, T. Torimaru, K. Sakamoto, Growth of oxide particles in FeCrAl-oxide dispersion strengthened steels at high temperature. J. Nucl. Mater. 493 (2017) 180-188.

[28] N. Oono, Q.X. Tang, S. Ukai, Oxide particle refinement in Ni-based ODS alloy. Mater. Sci. Eng. A 649 (2016) 250-253.

[29] C. Vailhé, D. Farkas, Shear faults and dislocation core structures in B2 CoAl. J. Mater. Res. 12 (1997) 2559-2570.

[30] P. Haas, F. Tran, P. Blaha, Calculation of the lattice constant of solids with semilocal functionals. Phys. Rev. B 79 (2009) 085104.

[31] R.O. Scattergood, D.J. Bacon, The Orowan mechanism in anisotropic crystals. Phil. Mag. A 31 (1975) 179-198.

[32] K.G. Field, M.A. Snead, Y. Yamamoto, K.A. Terrani, Handbook on the Material Properties of FeCrAl Alloys for Nuclear Power Production Applications, ORNL/TM-2017/186.

[33] D. Tabor, The hardness of metals, Oxford university press, 1951.

[34] H.Y. Yasuda, Y. Odawara, K. Soma, T. Yoshimoto, K. Cho. Effects of CoAl precipitates on deformation behavior of Fe-Al-Co single crystals. Intermetallics 91 (2017) 140-149.

[35] R.C. Reed, The superalloys Fundamentals and Applications, Cambridge University Press, 2006.

[36] A.J. Ardell. Precipitation hardening. Metall. Trans. A 16 (1985) 2131-2165.

[37] Y. Yamamoto, B.A. Pint, K.A. Terrani, K.G. Field, Y. Yang, L.L. Snead, Development and property evaluation of nuclear grade wrought FeCrAl fuel cladding for light water reactors. J. Nucl. Mater. 467 (2015) 703-716.

[38] C.P. Massey, S.N. Dryepondt, P.D. Edmondson, K.A. Terrani, S.J. Zinkle, Influence of mechanical alloying and extrusion conditions on the microstructure and tensile properties of Low-Cr ODS FeCrAl alloys. Nucl. Mater. 512 (2018) 227-238.

[39] Y. Zhang, S.C. Tonn, M.A. Crimp, Deformation structures in oriented NiAl and CoAl single crystals deformed at elevated temperature. Mat. Res. Soc. Symp. Proc. 288 (1992) 379-384.

[40] S. Takeuchi. Studies on ⟨100⟩ slip in Fe-2% V alloy single crystals. Jpn. J. Appl. Phys. 8 (1969) 1205-1210.

[41] G.Y. Chin. On ⟨100⟩ Versus ⟨111⟩ Slip in BCC Metals. Jpn. J. Appl. Phys. 9 (1970) 1260-1262.

[42] K.F. Hale, M.H. Brown, Experimental determination of Burgers vectors of dislocations. Proc. Roy. Soc. A 310 (1969) 479-491.

List of table

List of figures

Table 1 Lattice constants and misfit strain between B2 phase and matrix of 550-20-AT.

Sample ID	a_{B2} /Å	a_{BCC} /Å	δ /%
FCACO	2.959	2.952	0.24

Table 2 Average values of tensile properties tested at different temperatures.

Sample ID	YS/ MPa	UTS/ MPa	UE/ %	TE/ %
RT	1583	1642	1.4	1.4
300 °C	1329	1477	5.5	5.5
500 °C	667	703	0.7	6.6

Table 3 Detailed parameters for calculations.

Sample ID	r_o /nm	$\bar{r}$ /nm	$\overline{r^2}$ /nm^2	$\overline{r^3}$ /nm^3	r_s /nm	l_s /nm	f /%	λ /nm	D /nm	r /nm	B	u
Oxide particles	0.25~0.75	3.1	9.8	32.7	2.5	64.5	0.53	75.7	4.7	-	-	-
CoAl	-	-	-	-	-	-	11.4	-	-	3.6	0.11	0.29

Table 4 Calculation of strengthening stress from oxide particles and CoAl precipitates.

	RT	300 °C	500 °C
Measured UTS (MPa)	1642	1477	703
$\boldsymbol{\sigma_o}$ oxide dispersion strengthening (MPa)	415 ~ 603	386 ~ 560	353 ~ 512
$\boldsymbol{\sigma_{order}(1)}$ ordered strengthening (MPa)	425	454	488
$\boldsymbol{\sigma_{order}(2)}$ ordered strengthening (MPa)	425	442	461

Table 5 Visibility analysis of dislocations with different g-vectors near to [001] zone axis in tensile specimens. (● and ○ indicate that the dislocation is visible and invisible respectively)

g \ ***b***	***b***(×a)					
	[100]	[010]	1/2[111]	1/2[$\bar{1}$11]	1/2[1$\bar{1}$1]	1/2[11$\bar{1}$]
[110]	●	●	●	○	○	●
[1-10]	●	●	○	●	●	○
[020]	○	●	●	●	●	●
[200]	●	○	●	●	●	●

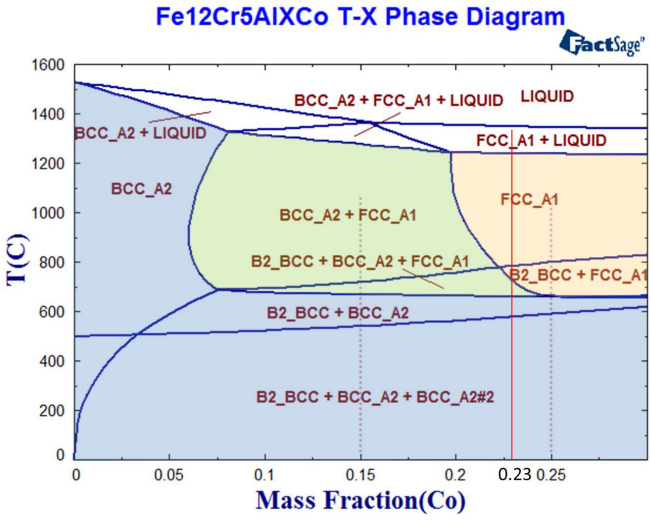

Fig. 1 Fe12Cr5Al-xCo pseudo binary phase diagrams computed using FactSage [22].

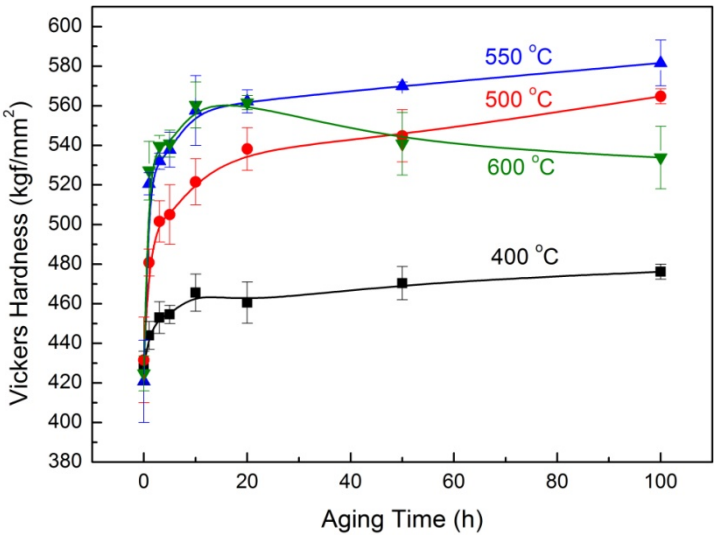

Fig. 2 Evolution of Vickers hardness as a function of ageing time.

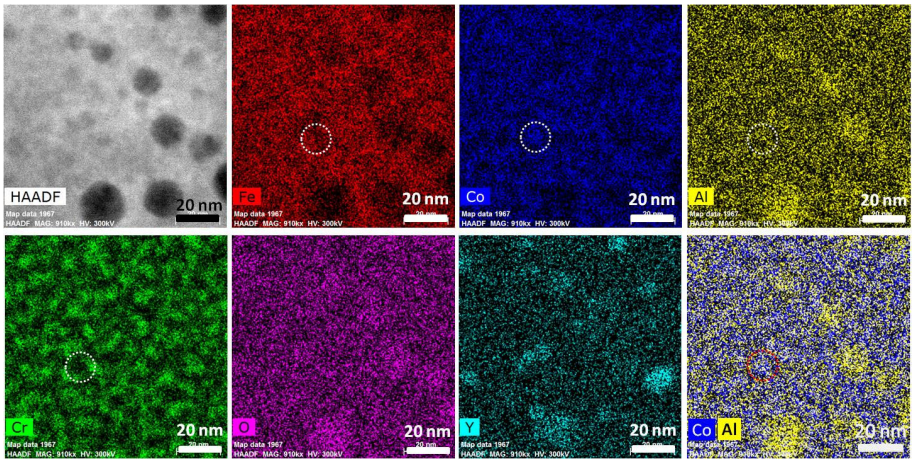

Fig. 3 HAADF image and corresponding elemental mappings of 550-20-AT obtained using a Titan-TEM.

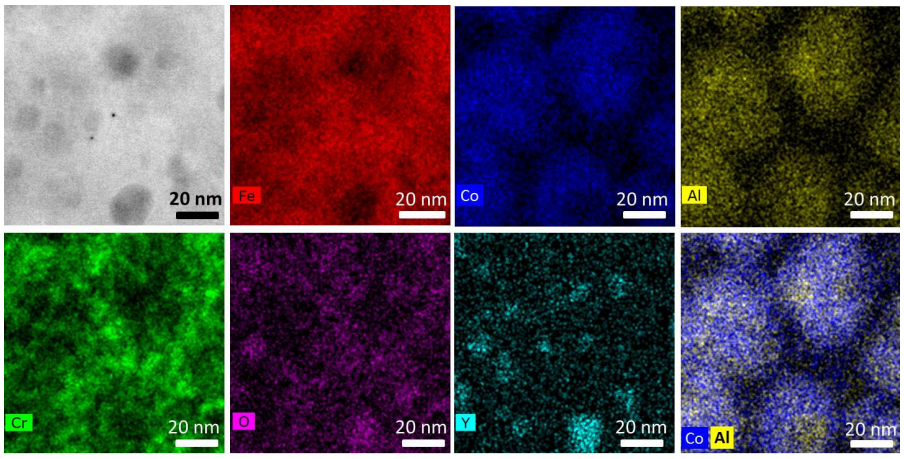

Fig. 4 HAADF image and corresponding elemental mappings of 600-100-AT obtained using a Titan-TEM.

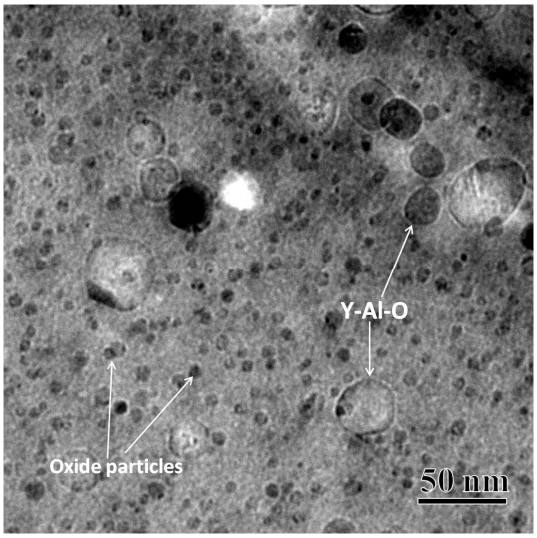

Fig. 5 Bright field image of oxide particles observed by TEM.

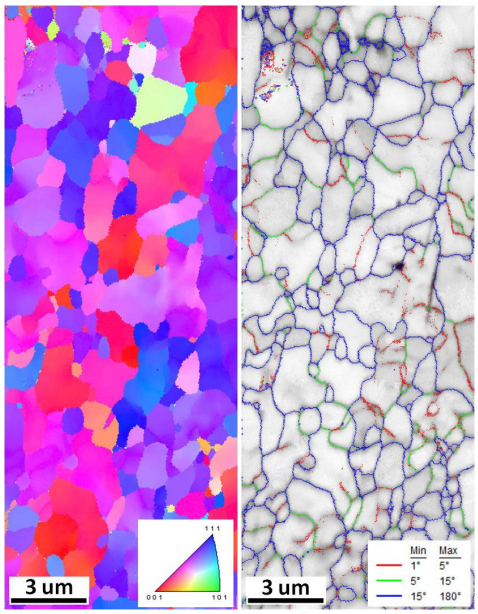

Fig. 6 IPF map and corresponding grain boundary map of 550-20-AT.

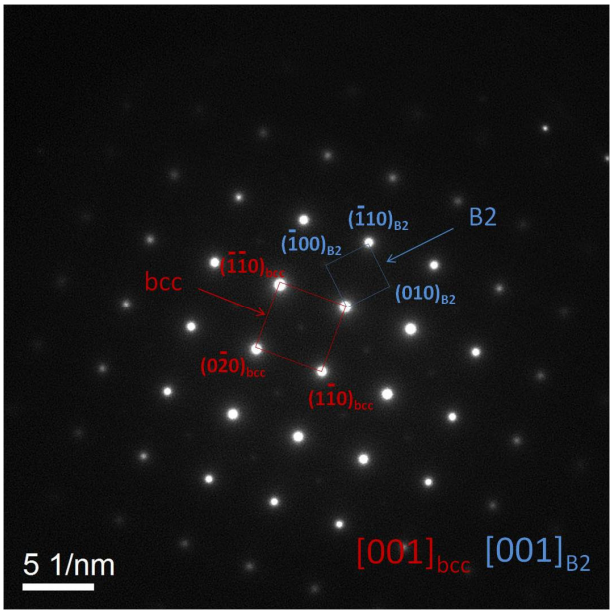

Fig. 7 Diffraction pattern of B2 phase and matrix in 550-20-AT obtained by TEM.

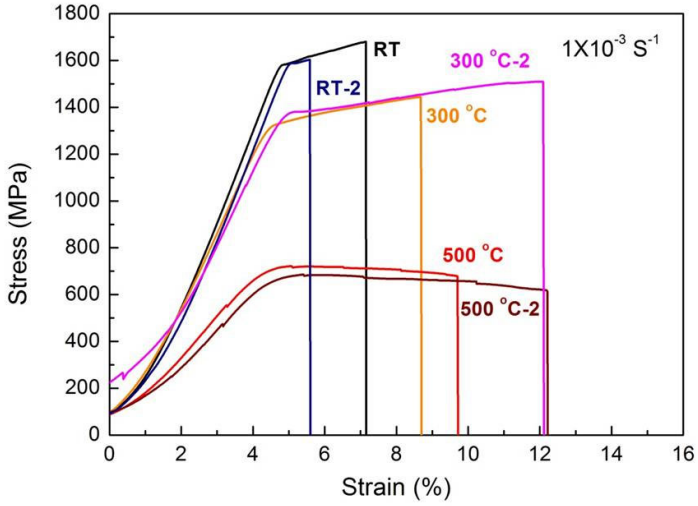

Fig. 8 S-S curves of 550-20-AT at RT, 300 °C, 500 °C.

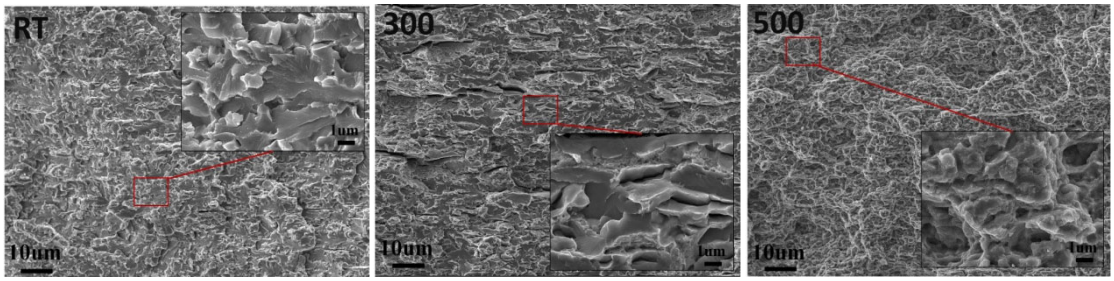

Fig. 9 Fracture surfaces of tensile specimens tested at RT, 300 °C and 500 °C.

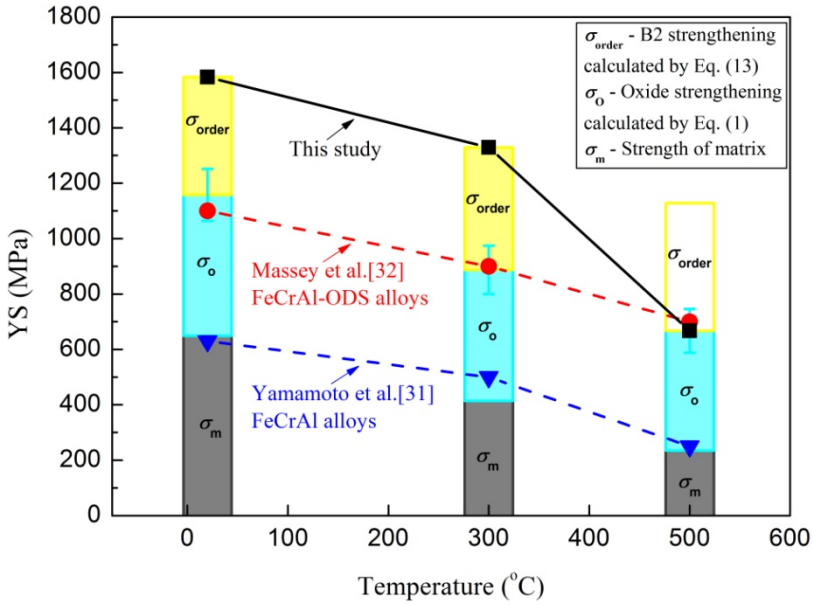

Fig. 10 Temperature dependency of order strengthening and oxide dispersion strengthening

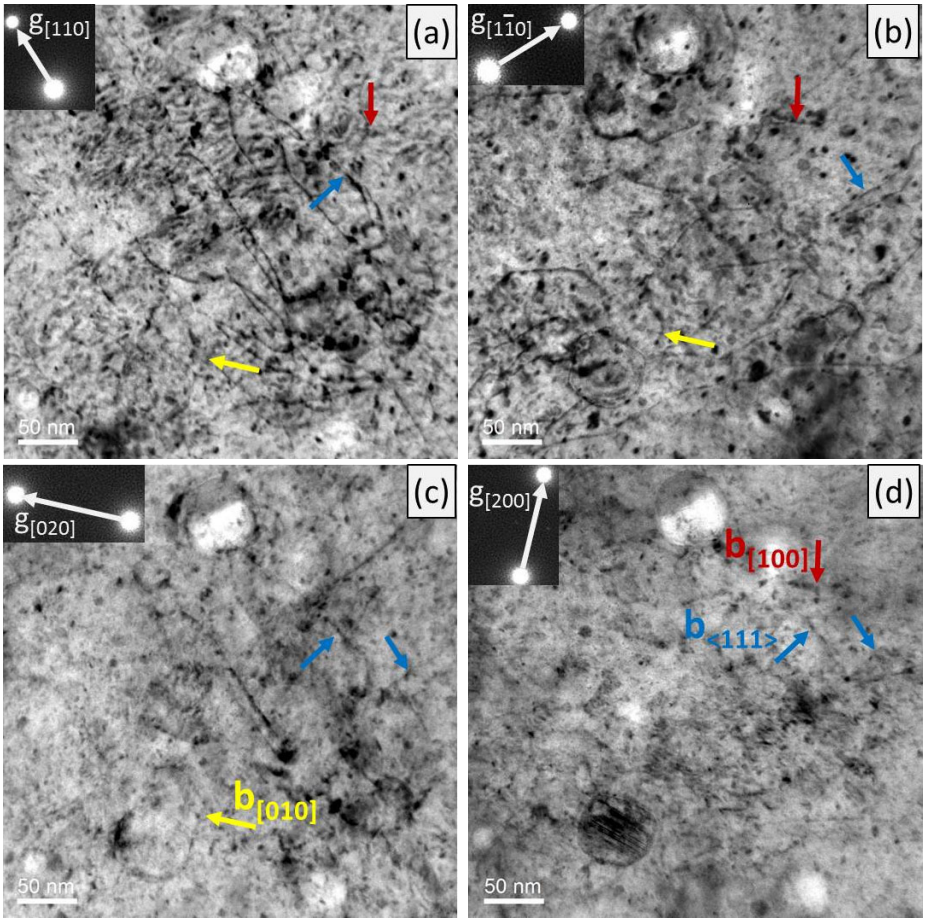

Fig.11 BF-TEM images of tensile specimen tested at 500 °C with four different g-vectors: a) [110], b) [1$\bar{1}$0], c) [020], d) [200], z-axis=[001].